Journal of Materials Chemistry A

PAPER

Check for updates

Cite this: J. Mater. Chem. A, 2019, 7, 20325

Homogeneous Li deposition through the control of carbon dot-assisted Li-dendrite morphology for high-performance Li-metal batteries†

Dongki Hong,‡[a] Yuri Choi,‡[b] Jaegeon Ryu,[c] Jinhong Mun,[b] Wooyeong Choi,[a] Minju Park,[a] Yongwon Lee,[a] Nam-Soon Choi,[a] Geunsik Lee,*[b] Byeong-Su Kim*[d] and Soojin Park*[c]

Received 12th June 2019
Accepted 1st August 2019

DOI: 10.1039/c9ta06260b

rsc.li/materials-a

Lithium metal as a battery anode is one of the most promising energy storage materials owing to its high theoretical capacity and low working potential. However, uncontrollable Li growth during cycling raises safety issues in the battery due to dendrite formation and a poor coulombic reversibility. Here, a design involving carbon nanodots (CDs) as electrolyte additives is introduced, which could significantly improve the morphology of the Li plating and cycling stability of lithium-metal batteries (LMBs). These CDs are suitable electrolyte additives because they show good dispersibility against organic solvents, originating from their 2–5 nm small-sized particles. In addition, CDs include surface negative charges and various functional groups, which are easily controllable through modulating the amount and types of precursors used. The surface negative charges and the functional groups in the CDs draw Li cations by electrostatic force and provide a strong Li-ion affinity. This synergistic combination enables uniform Li-ion transportation to the current collector, resulting in metal reduction with a smooth surface during the plating/stripping process. Moreover, the control of the CD-assisted Li dendrite morphology was examined by *ex situ* transmission electron microscopy. In the LMB full-cell tests with limited 20 μm-thick Li metal, the CD-containing electrolytes exhibited a capacity retention value of 99.9% after 100 cycles. Here, the CD-assisted Li deposition minimized the risks originating from Li dendrite growth, thus stabilizing the cycling ability of the LMB.

Introduction

With the demands for high energy density storage systems, replacing conventional graphite anodes in lithium-ion batteries provides a significant opportunity to resolve the limitations of a conventional battery in future applications. Among the diverse candidates, Li metal is a suitable choice owing to its high specific capacity (3860 mA h g^{-1}) and lowest redox potential (−3.04 V *vs.* standard hydrogen electrode).[1,2] However, thermodynamically unsteady states, for example, the rough surface of the current collector or the Li metal, cause a disordered Li deposition during cycling.[3,4] This dendritic growth of Li metal raises several critical issues, such as a low coulombic efficiency, electrolyte depletion, and safety concerns.[5] Thus, Li dendrite management has been widely studied in the past decades to attain stable Li metal batteries (LMBs).[6–8]

To address the risks originating from Li dendrite formation, several approaches for dendrite suppression have been proposed, such as an artificial solid-electrolyte interface (SEI) coating for depositing Li metal between the current collector and protecting layer,[9–14] a high-concentration ether-based electrolyte for smooth Li plating,[15–20] artificial structuring of the anode to cage the grown Li metal in the matrix,[21–25] and the introduction of electrolyte additives for building a stable interface.[26–30] The aforementioned strategies have accomplished significant progress, both in terms of morphology control and electrochemical performance. Nevertheless, it is still highly desirable to improve the insufficient battery performance compared to commercial Li-ion batteries as well as to provide a fundamental mechanistic analysis of Li dendrite suppression for the practical usage of Li metal anodes.[31,32]

The key element for the control of Li dendrite morphology lies in the homogeneous deposition of Li during the plating process.[33–35] Without any treatment, the uneven nucleation of Li

[a]School of Energy and Chemical Engineering, UNIST, 50 UNIST-gil, Ulsan 44919, Republic of Korea

[b]Department of Chemistry, School of Natural Science, UNIST, 50 UNIST-gil, Ulsan 44919, Republic of Korea. E-mail: gslee@unist.ac.kr

[c]Department of Chemistry, Division of Advanced Materials Science, Pohang University of Science and Technology (POSTECH), 77 Cheongam-Ro, Pohang 37673, Republic of Korea. E-mail: soojin.park@postech.ac.kr; Tel: +82-54-279-2102

[d]Department of Chemistry, Yonsei University, 50 Yonsei-ro, Seoul 03722, Republic of Korea. E-mail: bskim19@yonsei.ac.kr

† Electronic supplementary information (ESI) available. See DOI: 10.1039/c9ta06260b

‡ These authors contributed equally to this work.

deposition and the concomitant growth of needle-like Li metal results in battery failure when using conventional lithium hexafluorophosphate ($LiPF_6$)-containing carbon electrolytes, with the main issues being a continuous SEI/crack formation, electrolyte consumption, and a high cell resistance.[36–38] In this regard, the electrolyte additive strategy for dealing with dendrite formation provides a simple but universally applicable solution that could be applied to systematically control the nature of the interface and guide uniform metal deposition, which are promising for its feasibility on the industrial scale.[28–30] Although partial improvements in the Li growth morphology and the cyclability of LMBs using several additives have been reported, the battery performance and stability are still significantly short of reaching the required commercial level.[39] Therefore, new concepts of Li-ion adsorption materials (such as LMBs) have been proposed for the prevention of the disordered Li metal reduction by employing the strong affinity between Li ions and functional groups (Fig. 1).

Herein, we introduce nanoscale carbon dots or carbon nanodots (CDs) as an electrolyte additive for shuttling the Li-ions for achieving a uniform deposition of Li metal. Specifically, CDs are mass-producible in a single step from simple organic precursors and are highly dispersible in carbonate-containing electrolytes used for LMBs. The synergistic interplay between the highly negative surface charges and configuration of the nitrogen in CDs play a critical role in establishing a strong Li-ion affinity, as determined by various characterizations and computational analysis. This CD-based shuttling not only provides the nucleation sites for the Li-ions but also assists homogeneous Li plating, ultimately leading to an improvement

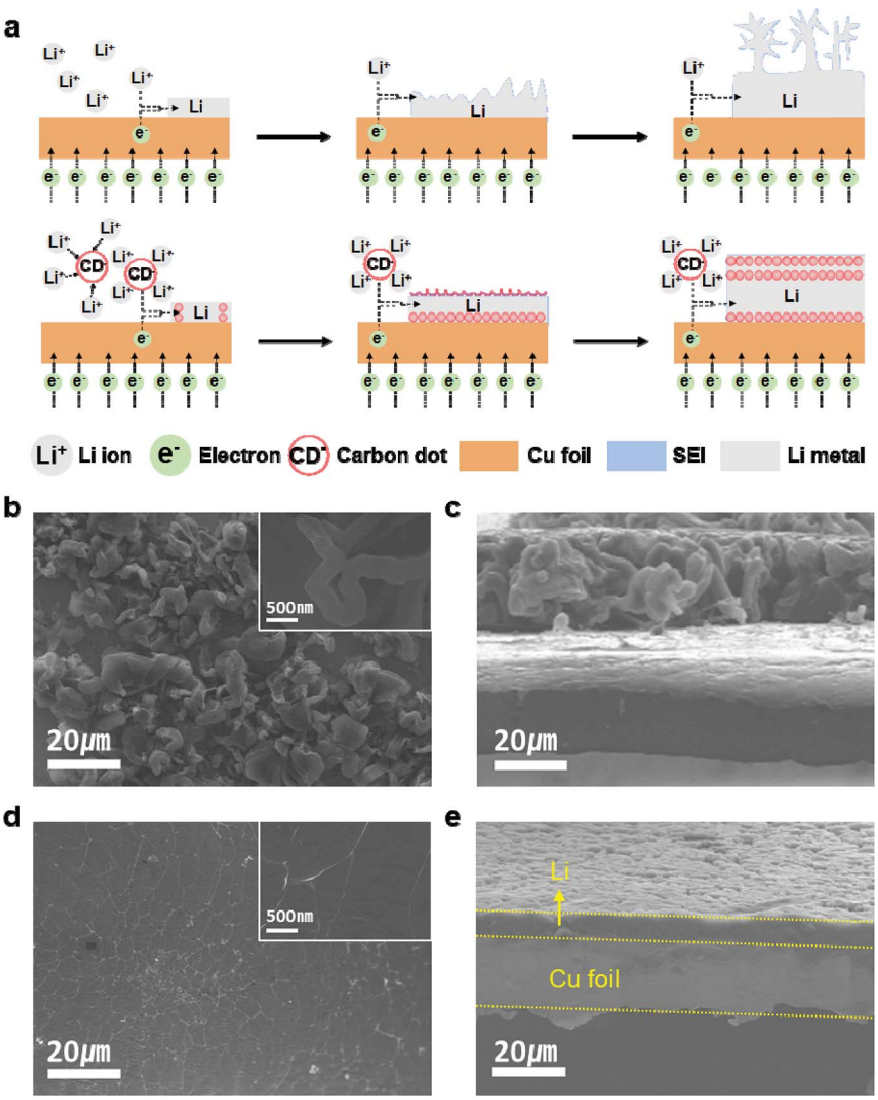

Fig. 1 Schematic and SEM images of the Li deposition behavior on Cu foil. (a) Schematic illustration of the Li deposition behavior with and without using carbon dot additives. (b and c) SEM images of Li dendrite growth without using the carbon dot additives; (b) Top view (b, inset: high magnification image) and (c) cross-sectional view. (d and e) SEM images of uniform Li deposition with the carbon dot additives; (d) Top view (d, inset: high magnification image) and (e) cross-sectional view. Scale bars are 20 μm (inset: 500 nm) (b–e). The test conditions of Li plating in the SEM images are a current density of 0.1 mA cm^{-2} and an areal capacity of 1 mA h cm^{-2}.

This journal is © The Royal Society of Chemistry 2019

of battery durability. We further performed *ex situ* transmission electron microscopy (TEM) analysis for unravelling the principles behind the CD-assisted Li dendrite morphology control. The CD-dispersed electrolytes showed enhanced electrochemical performances, delivering 95.5% of the average coulombic efficiency for 100 cycles in a Li/Cu half-cell, stable overpotential value for 500 cycles in a Li/Li symmetric-cell, and 99.9% capacity retention after 100 cycles for a 20 μm Li/cathode full-cell. Overall, the CD-assisted homogeneous Li deposition suggests a new design paradigm towards the practical usage of LMBs.

Experimental

Synthesis of the carbon nanodots

The CDs were synthesized by different carbonization methods. To prepare the N-CD, 960 mg of citric acid (5 mmol, Aldrich) and 347 mL of ethylene diamine (5 mmol) were dissolved in 10 mL of water under vigorous stirring for 2 min. The solution was then placed in a microwave oven (commercial microwave, 700 W) and heated for 2 min, and a yellow solid was obtained after cooling to room temperature. The solid was diluted in 5 mL of water. The yellow suspension was dialyzed (SpectraPor MWCO 500–1000) for 2 days to remove the salts and unreacted chemicals. For the preparation of the U-CD, 3 mmol of citric acid was dissolved in 10 mL of DMF.[40] Urea (10 mmol) was then added into the DMF solution, followed by a solvothermal reaction at 180 °C for 12 h in a sealed Teflon-lined autoclave. After cooling to room temperature, an excess of ethyl acetate was added to the solution to induce precipitation. After washing several times with a mixture of ethyl acetate and methanol, a black powder was obtained and dried in a vacuum oven.

Material characterization

The microstructural evolution was investigated *via* scanning electron microscopy (S-4800, Hitachi), TEM (JEM-2100, JEOL), STEM (Tecnai G2 F20 X-Twin, FEI), Raman spectroscopy (alpha300R, WITec), FT-IR analysis (670-IR, Varian), zeta-potential analysis (Zeta-Potential Analyser, Nano-ZS, Malvern), XPS (K-alpha, Thermo Fisher), and elemental analysis (Element Analyzer, Flash 2000, Thermo Fisher).

Density functional theory method

Structural optimization and total energy calculations were performed using Gaussian 09 at the level of PBE/6-31G*.[41,42] The equilibrium structure was confirmed by the absence of a negative frequency mode. For each optimized geometry of the functionalized CD with Li^+ bonded, the binding energy, defined as $E(\text{CD–Li}^+) - E(\text{CD}) - E(\text{Li}^+)$, was calculated with the basis set superposition error corrected by the counterpoise method.

Electrolyte preparation

A series of synthesized CDs was added to 5 mL of 1.3 M $LiPF_6$ ethylene carbonate/diethyl carbonate (EC/DEC, 3/7 vol%) solution under an argon atmosphere with the target concentration of 0.01–5 mg mL^{-1}. Then, vigorous stirring and ultrasonication were conducted for the uniform distribution of the CD particles. The achieved CD suspensions maintained the degree of dispersion for over a month, which enabled homogeneous Li plating.

Ex situ TEM measurements

Ex situ TEM analysis was performed with Li plating/stripping on a copper TEM grid. By using a 2032-coin type Li/Cu half-cell system and locating the TEM grid between the current collector and Li metal, electrochemical Li plating/stripping successfully occurred on the TEM grid. To determine the fundamental role of the U-CD, various states (bare, electrolyte dropping, rinsing, Li plating, Li stripping and Li re-plating) of the TEM grid with and without the U-CD were prepared. A series of TEM grids were obtained by disassembling the coin cells in an argon-filled glove box and then transporting them to the TEM holder.

Electrochemical characterization

Electrochemical tests were performed using a 2032 coin-type Li/Cu half-cell, Li/Li symmetric-cell and Li/cathode full-cell. The Li/Cu half-cell was composed of a Cu current collector, polymer separator (Celgard 2400), and a lithium electrode (20 μm, 300 μm thickness, Honjo). In the case of the symmetric-cell, the Cu current collector was substituted by 300 μm lithium. For the full-cell, a 20 μm-thick lithium electrode was combined with the $LiCoO_2$ (LCO, L&F Inc.) electrode. The LCO cathode consisted of 95 wt% of an active material, 2.5 wt% binder (polyvinylidene fluoride (PVDF, KUREHA KF 1100)), and 2.5 wt% super-P (TIMCAL), which was prepared by the slurry coating method with a loading level of ~7 mg cm^{-2}. The electrolyte was 1.3 M $LiPF_6$ solution in EC/DEC (3/7 vol%) with 0.01–5 mg mL^{-1} carbon dot additives included to improve the cycling stability. The operating conditions were 1.0 V stripping cut-off voltage with a specific capacity of 1 mA h cm^{-2} at a 0.1–1 C-rate for the Li/Cu half-cell, 0.5–1 mA h cm^{-2} at a 1–5 C-rate for the Li/Li symmetric-cell, and a 3.0–4.45 V voltage window with a 0.1–1 C-rate for the Li/LCO full-cell. The electrochemical properties were measured using a cycle tester (WBCS3000 battery systems, Wonatech) and an impedance tester (VMP3 EIS systems, Bio Logic).

Results and discussion

The chemical structures and related surface states of CDs can be tuned precisely with different types of precursors and synthetic protocols.[43] Accordingly, we prepared various CDs with different physical and chemical properties (Fig. 2a). A urea-based nitrogen-functionalized carbon nanodot (U-CD) was prepared through the solvothermal decomposition of citric acid and urea in *N*,*N*-dimethylformamide (DMF) (see the Experimental section for details). Additionally, we synthesized an ethylene diamine-based nitrogen-functionalized carbon nanodot (N-CD) by microwave pyrolysis using citric acid and ethylenediamine as reported in our previous study.[44] The as-synthesized CDs were indicated to be 2 to 5 nm in diameter, which was a great help to

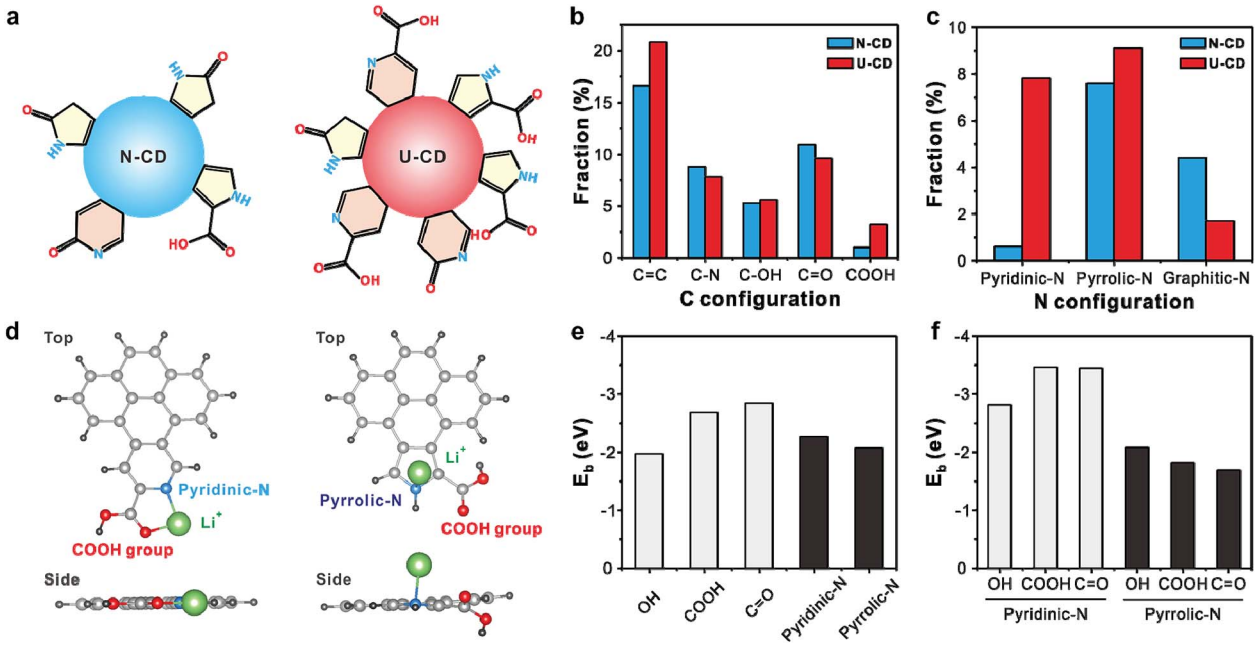

Fig. 2 Chemical properties of the carbon dot additives. (a) Structural illustration of the N-CD and U-CD. (b and c) Chemical compositions of the N-CD and U-CD determined by the high-resolution XPS spectra of C 1s (b) and N 1s (c), respectively. (d) Model structures for the binding energy calculation of a Li ion and functional groups, such as pyridinic-N, pyrrolic-N, and COOH. (e and f) The binding energy of the Li ions as a function of a single functional group (e) and dual functional groups (f).

secure the solvent dispersibility (Fig. S1†). After the purification process, all the CDs were well-dispersed in various concentrations (in the range of 0.01 to 5 mg mL^{-1}) of the carbonate electrolyte, without any noticeable precipitation for several months (Fig. S2†). The synthesized CDs presented negative ζ-potential values of -5.0 ± 1.6 (N-CD) and -25.1 ± 0.6 mV (U-CD) in water, suggesting the presence of negatively charged groups on the surface of the CDs (Fig. S3†). Moreover, Fourier transform infrared (FT-IR) spectroscopy was performed to identify the functional groups of the U-CD and N-CD (Fig. S4†). The FT-IR spectra revealed that both the U-CD and N-CD displayed a broad peak at 3222 cm^{-1}, corresponding to the O–H and N–H stretching. Interestingly, the peak intensity of carboxylic acid was considerably higher with the U-CD than that achieved with the N-CD at 1709 cm^{-1}, which is in accordance with the ζ-potential measurement.

Elemental analysis (EA) and X-ray photoelectron spectroscopy (XPS) measurements were performed to further investigate the chemical compositions and structures of the N-CD and U-CD. The major components of the N-CD and U-CD were determined to be C, N, and O (Fig. S5†). The deconvoluted C 1s and N 1s XPS spectra revealed the presence of O- and N-based functional groups in the CDs, which can serve as the interaction sites with Li ions (Fig. S6†). The high-resolution C 1s spectra yielded different fractions of the oxygen functional groups in the N-CD and U-CD (Fig. 2b and S7a†). The U-CD was found to contain 3.2% of the carboxylic acid groups (288.6 eV), whereas the N-CD only contained 1.0% of the carboxylic acid groups, which is in good agreement with the ζ-potential and FT-IR results.

It is well known that edge states related to both oxygen and nitrogen groups are critical for the formation of Li–CD clusters, such as pyrrolic-N and pyridinic-N, giving rise to the lone-pair states of N.[35] As shown in Fig. 2c and S7b,† the N-CD and U-CD include N configurations, such as pyrrolic-N, pyridinic-N, and graphitic-N. Interestingly, however, their fractions were significantly different for each CD. Specifically, pyrrolic-N (7.6%) and graphitic-N (4.4%) were dominant in the N-CD, whereas the U-CD included major contents of 9.1% of pyrrolic-N and 7.8% of pyridinic-N. This suggests that the combination of negative charges and abundant surface states allows the U-CD to provide more active sites for Li-ion absorption.

To prove this assignment, the binding energy of the interaction between the Li ions and functional groups of the CDs was calculated by the density functional theory (DFT) method (Note S1†). The structure of the CDs was simplified by placing different functional groups in a two-dimensional (2D) graphitic structure, albeit with the fact that its three-dimensional (3D) model allows a better description to understand the correlation between the Li ions and functional groups. Based on the combined experimental results from the EA and XPS and focusing on the most probable role of the edge functional groups, we constructed a small sp^2-carbon model, which possessed various distinct functional groups and structures, such as carbonyl, carboxylic, pyrrolic-N, and pyridinic-N groups (Fig. 2d and S8–S10†). First, we examined the binding effect between each functional group and Li ions. According to the DFT calculation of the O-related groups, functional groups such as carbonyl (−2.84 eV) and carboxylic (−2.68 eV) present in the

 This journal is © The Royal Society of Chemistry 2019

CDs are preferred for Li-ion absorption compared to the N-related groups (Fig. 2e). Among the N configurations, the pyridinic-N (−2.29 eV) had a slightly larger binding energy than the pyrrolic-N (−2.10 eV). The negative Mulliken charges of the respective O and N atoms (−0.62 for the ketone O, −0.60 for the pyridinic-N, and −0.58 for the pyrrolic-N) suggested that the major interaction was an ionic type. However, when a Li ion was placed between two distinct functional groups, the binding energy increased significantly, compared to that bonded to a single group, owing to a synergistic effect (Fig. 2f). In particular, the combination of the pyridinic-N and carboxylic acid groups was strong, as indicated by the strong binding energy of −3.45 eV, whereas the binding energy of the pyrrolic-N interaction with the carboxylic acid groups was only −1.80 eV (Table S1†). This is because the Li ions bonded to the pyridinic-N can form another ionic bond with a carbonyl group, which is not possible for pyrrolic-N due to the long distance to the nearby oxygen group. We, therefore, expect that the U-CD, which contained abundant carboxylic acid and pyridinic-N groups, could provide strong interaction and uniform nucleation sites for the Li ions.

Ex situ TEM was utilized to illuminate the role of the CDs during cycling.[45,46] Among the various CDs, we selected the U-CD owing to its strongest affinity for Li ions. To prepare the TEM sample, we used the electrochemical plating/stripping method performed on a Cu-based TEM grid instead of a Cu current collector. Various TEM samples (*e.g.*, bare grid, electrolyte dropping, rinsing, plating, and stripping) were designed for a thorough investigation of the Li growth morphology in the presence of the U-CD. As shown in Fig. S11,† the U-CD-dispersed electrolyte could not be adsorbed physically on the current collector without applying an electrochemical driving force.

To confirm the supporting effect of the U-CD, we observed the behavior of the Li plating/stripping with and without the U-CD through TEM and high-angle annular dark-field scanning transmission electron microscopy (HAADF-STEM) analysis. Li plating performed without the CDs resulted in a significant growth of the Li dendrite covering the entire grid with the development of a thick SEI layer (Fig. 3a–d). These disordered Li branches were broken during the stripping process and exposed to the reaction between the Li and electrolyte, resulting in continuous SEI formation and cracking, which, in turn, resulted in a low coulombic efficiency and poor cyclability (Fig. 3e–h). For the U-CD-containing electrolyte, strong interactions of the U-CD surface shuttled the Li ions to achieve a uniform Li plating. The corresponding TEM images exhibited a uniform distribution of approximately 2 to 5 nm-sized particles along the inner and outer surfaces of the grid with smooth Li stacking (Fig. 3i–l). The well-overlaid U-CD successfully suppressed dendrite growth without any side reaction, thereby yielding an immaculate Li surface and a stable SEI. More importantly, there were no macroscopic shape differences between the U-CD-aided plating and the stripping samples (Fig. 3i and m). The microscopic images and EDS analysis of the stripping with U-CD sample indicated the partially trapped U-CD by the remaining SEI shell. This shell represents a surface trace owing to the liberation of the surface-containing U-CD, which thereby decreases the density of the adsorbed U-CD (Fig. 3n, o and S12†). Furthermore, we verified that the partially desorbed U-CD was recyclable, and the examination of a series of TEM images indicated that there were few structural differences even after 100 cycles, which supports a long-term operation of the LMBs (Fig. S13†).

For further exploring the role of the CD additives, we performed electrochemical analysis. The first cycle galvanostatic voltage profiles of a Li/Cu half-cell test indicated that the overpotential values decreased in the order of the pristine electrolytes, N-CD, and U-CD (Fig. 4a). The initial coulombic efficiencies (ICEs) of the three samples were practically identical at approximately 95.0%; however, the cycling durability for each sample was distinguishable (Fig. S14†). This demonstrates that the CD additives reduced the cell resistance effectively during Li deposition, which could be attributed to the combination of the negative surface charges and the binding energy against the Li ions as determined by the DFT calculation. As such, the U-CD demonstrated the lowest overpotential and most stable cyclability, with an average coulombic efficiency of 95.5%. Moreover, Li/Li symmetric-cell tests were performed to verify the resistance decrease in the presence of the CD additives, and the results agreed well with the Li/Cu half-cell results obtained with a U-CD that had good cycling performance over 100 cycles (Fig. 4b and S15†). Further, we conducted Li/Li symmetric-cell tests under diverse concentrations for the U-CD from 0.01 to 5.0 mg mL^{-1} to determine the optimal conditions for the electrolyte (Fig. S16†). Here, 0.5 mg mL^{-1} of the U-CD concentration gave the best performance (Fig. 4c, S17 and S18, Table S2†). Specifically, the gap in voltage difference between each sample markedly widened as the cycle progressed (Fig. S19 and S20†). This is because the dilute sample cannot attract Li ions effectively, whereas an extremely high concentration of the CDs increases the cell resistance (Note S2†). To further explore the cell resistance behavior with and without CDs, electrochemical impedance spectroscopy measurements were performed. Nyquist plots of the sample without the CDs are summarized in Fig. 4d and show a sudden increase in the charge transfer resistance after 300 cycles, which corresponded with the symmetric-cell results. In the case of U-CD, the as-assembled coin cell showed a larger semi-circle than that of the sample without CD owing to the extra resistance from the introduction of the additives (Fig. 4e and S21†). However, the surface negative charge and high Li-ion binding energy in U-CD allowed reaching a low resistance value after several cycles. In addition, this charge transfer resistance converged to a value around 15 ohms and maintained this over 500 cycles.

The morphology of the Li deposited sample was investigated from various aspects. We inspected the cycled Li metal coin-cell in the absence and presence of the U-CD. For Li deposition on a Cu foil without the CDs, the agglomeration of Li metal occurs with cycle progression, whereas plating with the U-CD resulted in a uniform Li-metal distribution (Fig. S22†). These Li growth trends were also observed in the symmetric-cell (Fig. S23†). The

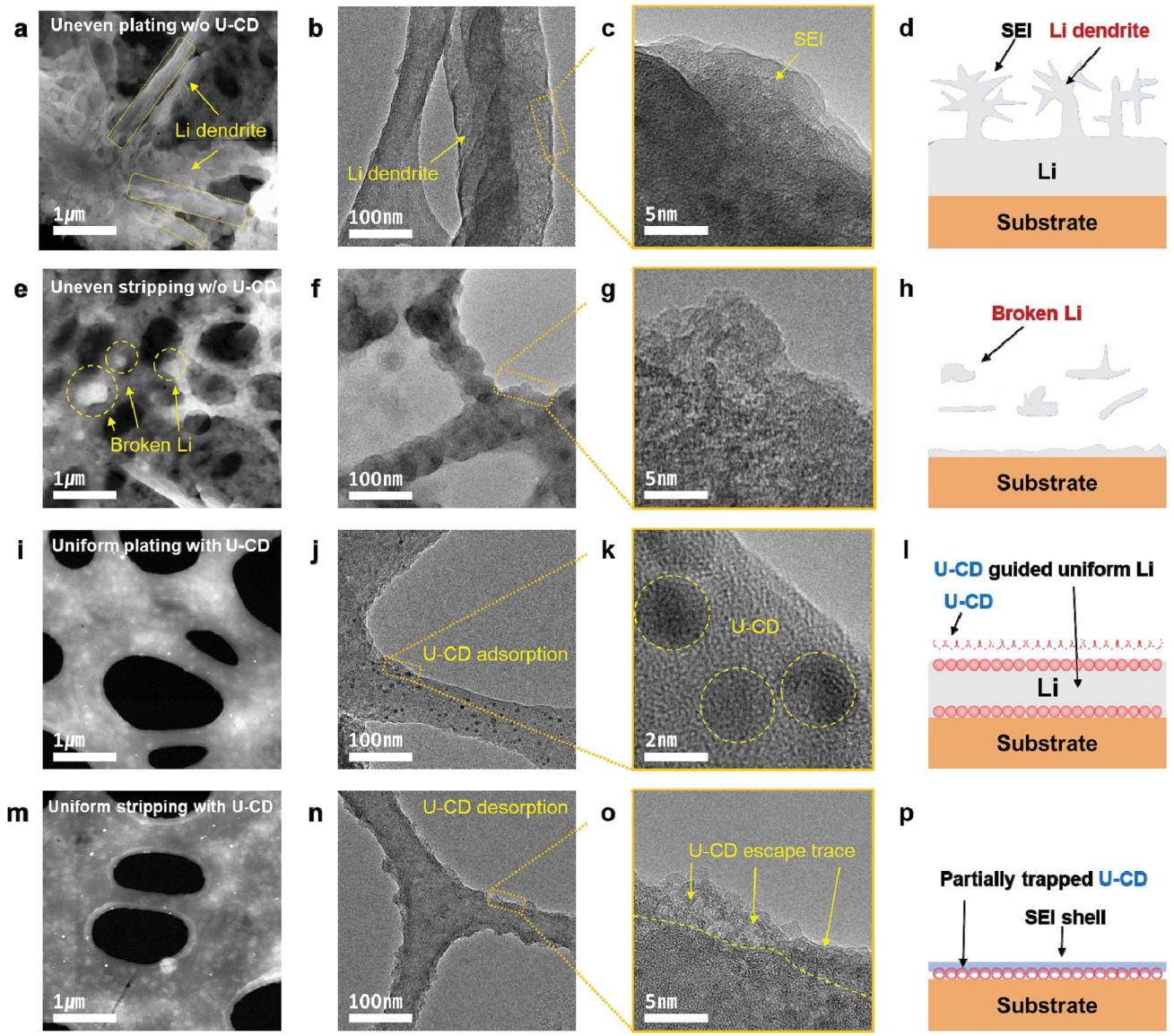

Fig. 3 The behavior of Li plating and stripping. A series of HAADF-STEM images, TEM images, and schematic illustrations of (a–d) plating without U-CD; (e–h) stripping without U-CD; (i–l) plating with the U-CD; and (m–p) stripping with the U-CD.

XPS spectra of the cycled Li metal exhibited a reduced overall peak intensity in the U-CD sample, which successfully prevented the formation of an extra SEI originating from the surface cracks and electrolyte decomposition (Fig. S24†).[30,47] Especially, N 1s spectra of cycled Li metal with U-CD tell us that the nitrogen functional groups of pyrrolic-N and pyridinic-N allow Li-ion affinity during cycling. In addition, the morphological differences were confirmed using scanning electron microscopy (SEM). The images of the sample without the U-CD additives displayed a broken Li array and thick degradation layer (Fig. 5a and c). In contrast, the U-CD allowed not only the suppression of Li dendrite growth but also the formation of a stable SEI with minimal electrolyte consumption and Li metal degradation (Fig. 5b and d). A smooth Li accumulation morphology assisted by the U-CD was observed and confirmed that the overpotential was closely related to the morphology of the Li layer. Lastly, we evaluated LMB full-cell with matching an ultrathin 20 μm-thick limited Li foil (approximately 4 mA h cm^{-2}) and a 1 mA h cm^{-2} of $LiCoO_2$ (LCO) cathode to confirm the practical usage of the LMB.[15] The ICE value was determined as 93.5% for the sample without the CD and 96.6% for the sample with the U-CD (Fig. 5e). The battery efficiency gap stood out during the cycling test, which showed that the average coulombic efficiency was 98.1% without the CD and 99.1% with the U-CD. In addition, after 100 cycles, the capacity retention of the system was 57.9% without the CD and 99.9% with the U-CD (Fig. 5f). The U-CD-aided outstanding battery improvement was also verified under manifold cycling conditions (Fig. S25†).

The well-designed nitrogen-functionalized CDs, which include tunable surface charges and binding energy, exhibited Li dendrite suppression ability and better electrochemical

 This journal is © The Royal Society of Chemistry 2019

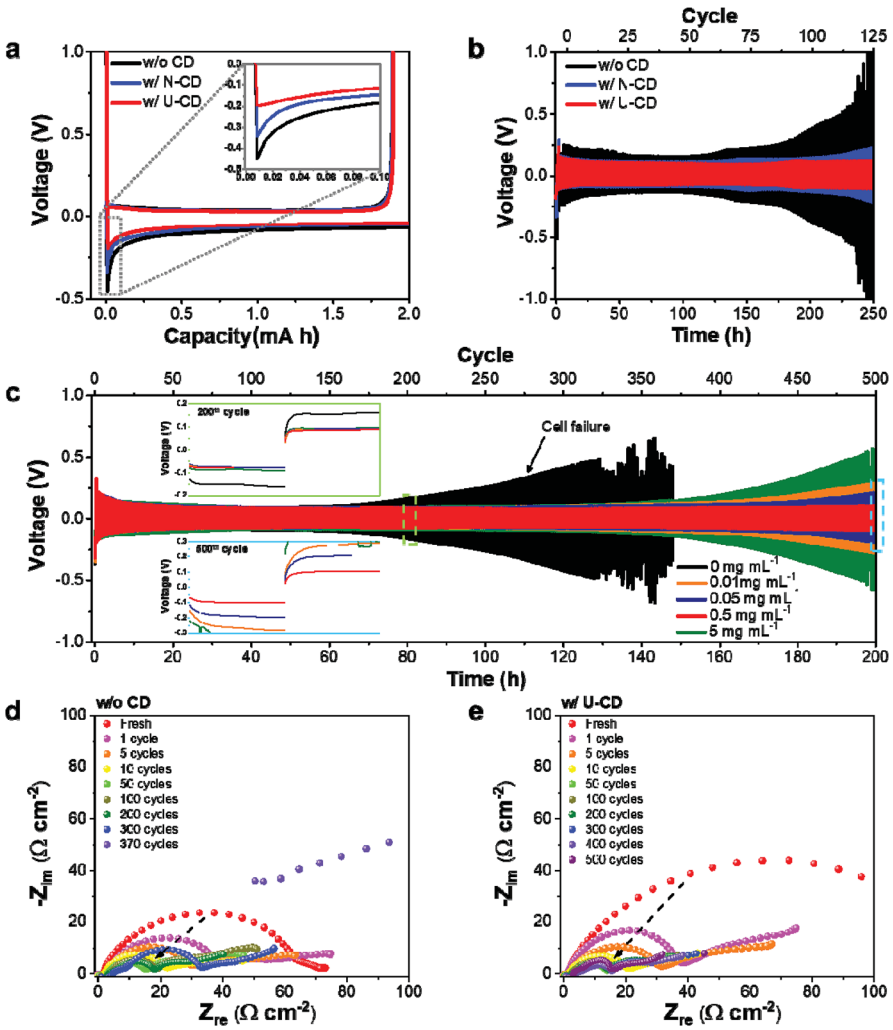

Fig. 4 Overpotential minimization through U-CD additives. (a) Initial galvanostatic voltage profiles of a Li/Cu half-cell. (b and c) Cycle retention properties of a Li/Li symmetric-cell: (b) at a current density of 1 mA cm^{-2} with an areal capacity of 1 mA h cm^{-2} and (c) at a current density of 2.5 mA cm^{-2} with an areal capacity of 0.5 mA h cm^{-2} in various electrolyte concentrations. (d and e) Nyquist plots of the impedance spectra behavior depending on the cycle progress: (d) without CD and (e) with U-CD. The CD concentration in the electrolyte was 0.5 mg mL^{-1} (a, b, and e).

performance in the role of an electrolyte additive. This CD effectively guided the Li plating and stripping processes as follows: the combination of the surface negative charges of the CD and the strong binding energy of the Li ions to the various carbon and nitrogen configurations attracted the Li ions by electrostatic forces at the initial stage of the electrochemical tests. It also built CD–Li-ion clusters, resulting in the enhancement of the Li-ion shuttle ability. Therefore, the CD–Li-ions moved together toward the current collector under the electric field, and the solution flowed during the plating. In this stage, the CD–Li-ion groups were affected by the repulsive forces against each other, resulting in a uniform distribution on the current collector.

The well-guided Li ions adjacent to the current collector accept electrons and are reduced to Li metal with the confinement of the CDs. This reduced Li metal is affected by the initial nuclei size, which causes Li-metal surface fluctuation. Thus, minimizing the seed size is critical for obtaining a uniform deposition. As 2–5 nm-sized CDs are well-distributed in the entire system, homogeneous Li stacking can occur with uniform SEI formation. In the process of Li stripping, the solid-phase Li returns to its ionic state by losing electrons with the escape of the trapped CDs. However, basically, the CDs cannot penetrate the SEI; therefore, only the outer-surface-adsorbed particles re-disperse into the electrolyte, leaving a porous interface trace. These CDs reunite with the Li ions owing to the electric force and can be used reversibly during cycling. From these results, we revalidated that the functionalized U-CDs operate well regardless of the cell types, such as a half-cell, symmetric-cell, and even a full-cell, because of the uniform Li plating/stripping induction. We anticipate that the U-CDs can be applied to other types of LMB systems owing to their synthetic feasibility, superior dispersity in conventional electrolytes, and compatibility under battery operating conditions, thus presenting a significant potential for practical usage.

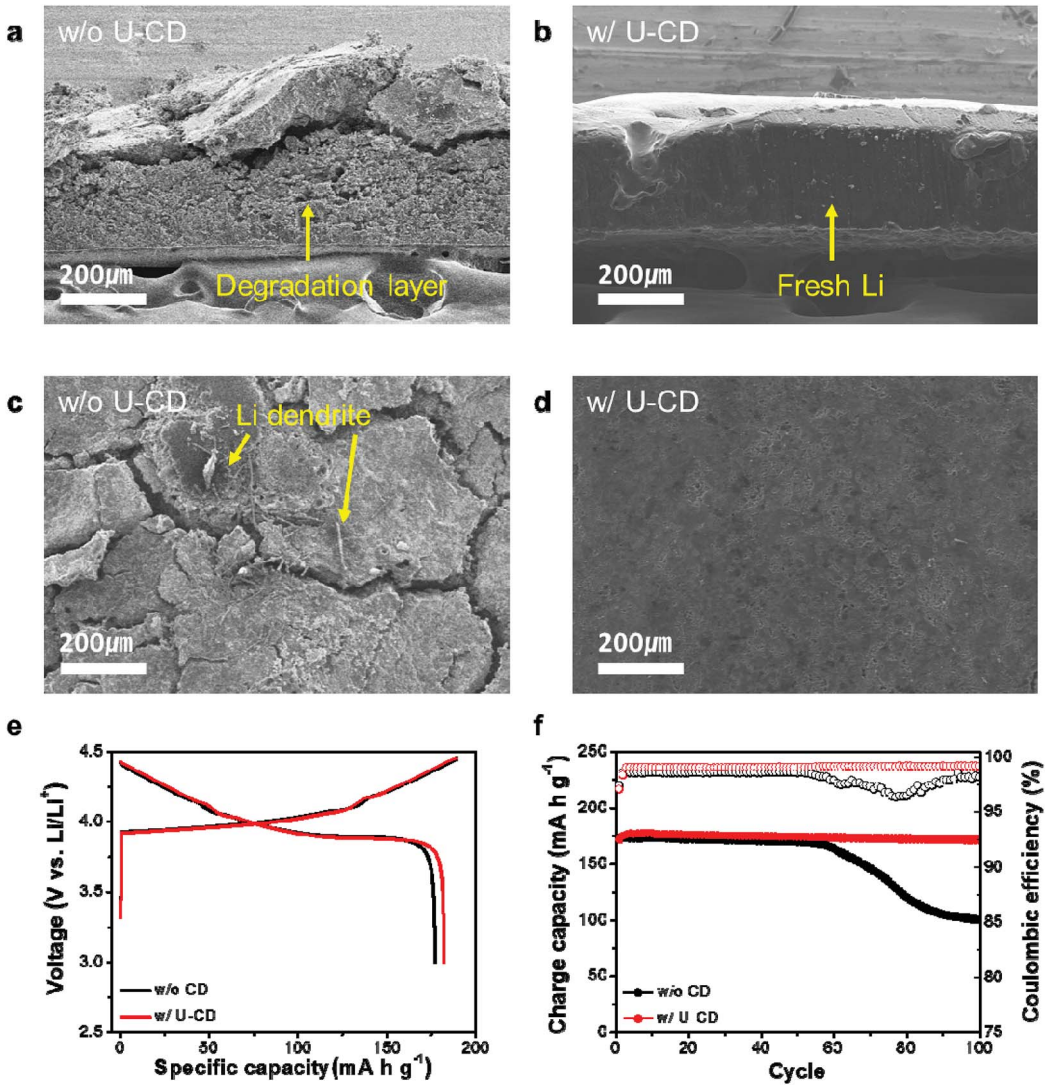

Fig. 5 Stable electrochemical performances originating from the carbon dot-assisted plating. A series of SEM images of the Li metal (a, c) without the CD after 370 cycles; (b, d) with the U-CD after 500 cycles. (e) First-cycle voltage profile of the Li/LCO full-cell. (f) Cycle retention properties of the 20 μm Li/LCO full-cell test at a current density of 1 mA cm^{-2} with an areal capacity of 1 mA h cm^{-2}. Scale bars are 200 μm (a–d). The electrolyte concentration was 0.5 mg mL^{-1}.

Conclusions

To summarize, we suggest single-step, mass-producible, and function-tunable CDs as electrolyte additives for LMBs. The CDs contain diverse carbon and nitrogen functional groups, which are highly controllable by modifying the ratio of the organic precursors, leading to variable surface charge states and Li-ion binding energy. The functionalized CDs exhibited tremendous potential for the suppression of unsteady Li deposition and display advanced electrochemical performances, which were attributed to the combination of the surface electric attraction force and strong Li-ion affinity. Specifically, the small size of the CDs induces small initial Li nuclei, resulting in ideal Li stacking with a stable SEI. From the TEM analysis, we checked the effect of the CDs against Li growth. The 2–5 nm-sized CDs were homogeneously distributed with smooth Li metal in the CD-assisted plating/stripping state, while a disordered Li dendrite mostly occurred in the non-assisted plating/stripping. This unique advancement of the CDs was also investigated in battery cycling tests. The Li/Cu half-cell tests conducted with the CDs delivered the lowest overpotential and a 95.5% average coulombic efficiency for 100 cycles under the cycling conditions of 1 mA cm^{-2} and 1 mA h cm^{-2}, whereas the results without the CDs showed an average coulombic efficiency of only 89.0%. In addition, the stable cycling of the CD-assisted Li/Li symmetric-cell tests continued up to 500 cycles under the condition of 0.5 mA h cm^{-2} and 2.5 mA cm^{-2}. In contrast, the potential difference with the pure Li/Li symmetric-cell had already increased drastically before approaching 200 cycles. Even under extreme conditions of a 20 μm limited Li metal anode with an LCO cathode full-cell test, to which CD additives were applied, a 99.1% average coulombic efficiency for 100 cycles and 99.9%

This journal is © The Royal Society of Chemistry 2019

capacity retention after 100 cycles were delivered (98.1% average coulombic efficiency, 57.9% capacity retention without CDs). The outstanding electrochemical performance originated from the surface charges and high Li-ion binding energy of the CDs-based Li-metal morphology control. One of the strengths of the electrolyte additive studied is its good applicability, presenting a high potential in an industrial setup. Therefore, the systematic borderless CD additive-guided uniform Li plating will provide a new design paradigm for future LMBs.

Conflicts of interest

There are no conflicts to declare.

Acknowledgements

This work was supported by Technology Development Program to Solve Climate Changes through the National Research Foundation of Korea (NRF) funded by the Ministry of Science, ICT (2018M1A2A2063346). This work was supported by the National Research Foundation of Korea (NRF-2017R1A2B3012148 and NRF-2018R1A5A1025208).

References

1 J. M. Tarascon and M. Armand, *Nature*, 2001, **414**, 359–367.
2 D. C. Lin, Y. Y. Liu and Y. Cui, *Nat. Nanotechnol.*, 2017, **12**, 194–206.
3 A. Kushima, K. P. So, C. Su, P. Bai, N. Kuriyama, T. Maebashi, Y. Fujiwara, M. Z. Bazant and J. Li, *Nano Energy*, 2017, **32**, 271–279.
4 S. H. Yu, X. Huang, J. D. Brock and H. D. Abruna, *J. Am. Chem. Soc.*, 2019, **141**, 8441–8449.
5 K. Shen, Z. Wang, X. Bi, Y. Ying, D. Zhang, C. Jin, G. Hou, H. Cao, L. Wu, G. Zheng, Y. Tang, X. Tao and J. Lu, *Adv. Energy Mater.*, 2019, **9**, 1900260.
6 R. Zhang, N. W. Li, X. B. Cheng, Y. X. Yin, Q. Zhang and Y. G. Guo, *Adv. Sci.*, 2017, **4**, 1600445.
7 H. Ye, S. Xin, Y. X. Yin and Y. G. Guo, *Adv. Energy Mater.*, 2017, **7**, 1700530.
8 Y. Y. Lu, Z. Y. Tu and L. A. Archer, *Nat. Mater.*, 2014, **13**, 961–969.
9 X. B. Cheng, C. Yan, X. Chen, C. Guan, J. Q. Huang, H. J. Peng, R. Zhang, S. T. Yang and Q. Zhang, *Chem*, 2017, **2**, 258–270.
10 M. S. Kim, J. H. Ryu, Deepika, Y. R. Lim, I. W. Nah, K. R. Lee, L. A. Archer and W. I. Cho, *Nat. Energy*, 2018, **3**, 889–898.
11 N. W. Li, Y. Shi, Y. X. Yin, X. X. Zeng, J. Y. Li, C. J. Li, L. J. Wan, R. Wen and Y. G. Guo, *Angew. Chem., Int. Ed.*, 2018, **57**, 1505–1509.
12 N. W. Li, Y. X. Yin, C. P. Yang and Y. G. Guo, *Adv. Mater.*, 2016, **28**, 1853–1858.
13 Y. Y. Liu, D. C. Lin, P. Y. Yuen, K. Liu, J. Xie, R. H. Dauskardt and Y. Cui, *Adv. Mater.*, 2017, **29**, 1605531.
14 M. D. Tikekar, S. Choudhury, Z. Y. Tu and L. A. Archer, *Nat. Energy*, 2016, **1**, 1–7.
15 S. R. Chen, J. M. Zheng, D. H. Mei, K. S. Han, M. H. Engelhard, W. G. Zhao, W. Xu, J. Liu and J. G. Zhang, *Adv. Mater.*, 2018, **30**, 1706102.
16 S. H. Jiao, X. D. Ren, R. G. Cao, M. H. Engelhard, Y. Z. Liu, D. H. Hu, D. H. Mei, J. M. Zheng, W. G. Zhao, Q. Y. Li, N. Liu, B. D. Adams, C. Ma, J. Liu, J. G. Zhang and W. Xu, *Nat. Energy*, 2018, **3**, 739–746.
17 J. F. Qian, B. D. Adams, J. M. Zheng, W. Xu, W. A. Henderson, J. Wang, M. E. Bowden, S. C. Xu, J. Z. Hu and J. G. Zhang, *Adv. Funct. Mater.*, 2016, **26**, 7094–7102.
18 J. F. Qian, W. A. Henderson, W. Xu, P. Bhattacharya, M. H. Engelhard, O. Borodin and J. G. Zhang, *Nat. Commun.*, 2015, **6**, 6362.
19 X. D. Ren, S. R. Chen, H. Lee, D. H. Mei, M. H. Engelhard, S. D. Burton, W. G. Zhao, J. M. Zheng, Q. Y. Li, M. S. Ding, M. Schroeder, J. Alvarado, K. Xu, Y. S. Meng, J. Liu, J. G. Zhang and W. Xu, *Chem*, 2018, **4**, 1877–1892.
20 L. M. Suo, Y. S. Hu, H. Li, M. Armand and L. Q. Chen, *Nat. Commun.*, 2013, **4**, 1481.
21 S. F. Liu, X. H. Xia, Y. Zhong, S. J. Deng, Z. J. Yao, L. Y. Zhang, X. B. Cheng, X. L. Wang, Q. Zhang and J. P. Tu, *Adv. Energy Mater.*, 2018, **8**, 1702322.
22 K. Yan, Z. D. Lu, H. W. Lee, F. Xiong, P. C. Hsu, Y. Z. Li, J. Zhao, S. Chu and Y. Cui, *Nat. Energy*, 2016, **1**, 16010.
23 C. P. Yang, Y. X. Yin, S. F. Zhang, N. W. Li and Y. G. Guo, *Nat. Commun.*, 2015, **6**, 8058.
24 W. D. Zhang, H. L. Zhuang, L. Fan, L. N. Gao and Y. Y. Lu, *Sci. Adv.*, 2018, **4**, eaar4410.
25 P. C. Zou, Y. Wang, S. W. Chiang, X. Y. Wang, F. Y. Kang and C. Yang, *Nat. Commun.*, 2018, **9**, 464.
26 W. Y. Li, H. B. Yao, K. Yan, G. Y. Zheng, Z. Liang, Y. M. Chiang and Y. Cui, *Nat. Commun.*, 2015, **6**, 7436.
27 X. Li, J. M. Zheng, X. D. Ren, M. H. Engelhard, W. G. Zhao, Q. Y. Li, J. G. Zhang and W. Xu, *Adv. Energy Mater.*, 2018, **8**, 1703022.
28 X. Q. Zhang, X. B. Cheng, X. Chen, C. Yan and Q. Zhang, *Adv. Funct. Mater.*, 2017, **27**, 1605989.
29 W. G. Zhao, L. F. Zou, J. M. Zheng, H. P. Jia, J. H. Song, M. H. Engelhard, C. M. Wang, W. Xu, Y. Yang and J. G. Zhang, *ChemSusChem*, 2018, **11**, 2211–2220.
30 J. M. Zheng, M. H. Engelhard, D. H. Mei, S. H. Jiao, B. J. Polzin, J. G. Zhang and W. Xu, *Nat. Energy*, 2017, **2**, 17012.
31 X. Fan, L. Chen, O. Borodin, X. Ji, J. Chen, S. Hou, T. Deng, J. Zheng, C. Yang, S. C. Liou, K. Amine, K. Xu and C. Wang, *Nat. Nanotechnol.*, 2018, **13**, 715–722.
32 L. Suo, W. Xue, M. Gobet, S. G. Greenbaum, C. Wang, Y. Chen, W. Yang, Y. Li and J. Li, *Proc. Natl. Acad. Sci. U. S. A.*, 2018, **115**, 1156–1161.
33 R. Zhang, S. Wen, N. Wang, K. Qin, E. Liu, C. Shi and N. Zhao, *Adv. Energy Mater.*, 2018, **8**, 1800914.
34 Y. Liu, B. Li, J. Liu, S. Li and S. Yang, *J. Mater. Chem. A*, 2017, **5**, 18862–18869.
35 R. Zhang, X. R. Chen, X. Chen, X. B. Cheng, X. Q. Zhang, C. Yan and Q. Zhang, *Angew. Chem., Int. Ed.*, 2017, **56**, 7764–7768.

36 X. Fan, X. Ji, F. Han, J. Yue, J. Chen, L. Chen, T. Deng, J. Jiang and C. Wang, *Sci. Adv.*, 2018, **4**, eaau9245.
37 W. Tang, X. Yin, S. Kang, Z. Chen, B. Tian, S. L. Teo, X. Wang, X. Chi, K. P. Loh, H. W. Lee and G. W. Zheng, *Adv. Mater.*, 2018, **30**, 1801745.
38 X. Wang, W. Zeng, L. Hong, W. Xu, H. Yang, F. Wang, H. Duan, M. Tang and H. Jiang, *Nat. Energy*, 2018, **3**, 227–235.
39 X. B. Cheng, M. Q. Zhao, C. Chen, A. Pentecost, K. Maleski, T. Mathis, X. Q. Zhang, Q. Zhang, J. J. Ziang and Y. Gogotsi, *Nat. Commun.*, 2017, **8**, 336.
40 Z. Tian, X. Zhang, D. Li, D. Zhou, P. Jing, D. Shen, S. Qu, R. Zboril and A. L. Rogach, *Adv. Opt. Mater.*, 2017, **5**, 1700416.
41 M. J. Frish, G. W. Trucks, H. B. Schlegel, G. E. Scuseria, M. A. Robb, J. R. Cheeseman, G. Scalmani, V. Barone, G. A. Petersson, H. Nakatsuji, *et al.*, *Gaussian 09, Revision D.01*, Gaussian, Inc., Wallingford CT, 2009.
42 J. P. Perdew, K. Burke and M. Ernzerhof, *Phys. Rev. Lett.*, 1996, **78**, 3865–3868.
43 Y. Choi, Y. Choi, O. H. Kwon and B. S. Kim, *Chem.–Asian J.*, 2018, **13**, 586–598.
44 Y. Choi, B. Kang, J. Lee, S. Kim, G. T. Kim, H. Kang, B. R. Lee, H. Kim, S. H. Shim, G. Lee, O. H. Kwon and B. S. Kim, *Chem. Mater.*, 2016, **28**, 6840–6847.
45 Y. Z. Li, Y. B. Li, A. L. Pei, K. Yan, Y. M. Sun, C. L. Wu, L. M. Joubert, R. Chin, A. L. Koh, Y. Yu, J. Perrino, B. Butz, S. Chu and Y. Cui, *Science*, 2017, **358**, 506–510.
46 Y. Li, W. Huang, Y. Li, A. Pei, D. T. Boyle and Y. Cui, *Joule*, 2018, **2**, 2167–2177.
47 S. Jiao, J. Zheng, Q. Li, X. Li, M. H. Engelhard, R. Cao, J. G. Zhang and W. Xu, *Joule*, 2018, **2**, 110–124.

 This journal is © The Royal Society of Chemistry 2019